Modeling the Impact of Metallic Ion Layers on Equatorial Spread F with SAMI3/ESF

J.D.Huba¹, J. Krall², and D. Drob²

 $^{\rm 1}$ Syntek Technologies, Fairfax, VA

² Naval Research Laboratory, Washington, DC

Abstract

The impact of E region metal ion layers on the development of equatorial plasma bubbles is investigated using the SAMI3/ESF model. We find that metal ion layers reduce the growth rate of the generalized Rayleigh-Taylor instability (GRTI) and act to suppress the development of equatorial plasma bubbles. This is consistent with theoretical expectations and observations, and is attributed to the increase in both the Pedersen and Hall conductances. Additionally, inhomogeneities in the E region metal ion layer can map into the F layer and alter the morphology of ESF bubble evolution. Lastly, we find that if equatorial spread F bubbles develop in the presence of a metal ion layer, then the electric fields generated by the instability can lift the metal ions into the F region. This is consistent with observations of Fe⁺ in the F region during equatorial spread F.

1 INTRODUCTION

Post-sunset ionospheric irregularities in the equatorial F region were first observed by Booker and Wells (1938) using ionosondes. The ionosonde trace of the reflected radio wave from the bottomside ionosphere is normally sharp and increases in altitude up to the F peak. However, Booker and Wells (1938) observed that after sunset the trace was often no longer sharp, but broadened in altitude over tens of kilometers. They attributed this observation to the formation of 'electron clouds with scale sizes of 30 meters.' This phenomenon eventually became known as equatorial spread F (ESF).

It is now known that during ESF the equatorial ionosphere becomes unstable because of a Rayleigh-Taylor-like instability: large scale (10s km) electron density 'bubbles' can develop and rise to high altitudes (1000 km or greater at times) [Haerendel, 1974; Ossakow, 1981; Hysell, 2000]. Understanding and modeling ESF is very important because of its impact on space weather: it causes radio wave scintillation that degrades communication and navigation systems. In fact, it was the focus of of the Air Force Communications/Navigation Outage Forecast Satellite (C/NOFS) mission [de La Beaujardiere, 2004].

One of the outstanding problems associated with equatorial spread F and plasma bubble development is the day-to-day variability of this phenomenon [Basu et al., 2009]. In fact, often times the ionosphere appears identical from one day to the next, yet spread F occurs on one day but not the other [e.g., Hysell et al., 2015]. One suggestion posited to suppress ESF is the stabilizing effect of transhemispheric neutral winds [Maruyama et al., 1988; Krall et al., 2009] on the generalized Rayleigh-Taylor instability (GRTI) [Haerendel, 1974; Sultan, 1996]. However, there are situations where these winds can actually increase the growth rate of the the GRTI [Huba and Krall, 2013]. Another possibility is the occurrence of sporadic E: studies have suggested that sporadic E suppresses equatorial spread F because of the enhanced

Pedersen conductance [Stephan et al., 2002]. In this regard we note that the metallic ions (e.g., Fe⁺ and Mg⁺) associated with meteoritic deposition in the E region have been suggested as a cause of the long-lasting nighttime E layer [Nicolet, 1955] as well as sporadic E events [Haldoupis, 2011]. Interestingly, Hanson and Sanatani (1971), reported observations that suggest an 'intimate relationship between the presence of Fe⁺ ions and irregularities in the total ion composition.' They note that 'whereas Fe⁺ is often present without irregularities, the reverse seldom occurs. This suggests that the presence of Fe⁺ is one of several conditions that must be satisfied to generate the irregularities.'

In this Letter we use the SAMI3/ESF model to investigate the impact of metallic ions (Fe $^+$ and Mg $^+$) on the onset and evolution of equatorial spread F. We find that the increase in the Pedersen conductance associated with metallic ion layers can reduce the growth rate of the GRTI. This is consistent with linear theory [Haerendel, 1974; Sultan, 1996]. However, we also find that the increase in the Hall conductance can also act to suppress the instability. In addition, spatial inhomogeneities in metal ion layers can impact morphology of bubble evolution. With regard to the observations reported in Hanson and Sanatani (1971) metallic ions appear to be 'tracers' of the electrodynamics associated with equatorial plasma bubbles; their presence is not required to generate the irregularities as they originally hypothesized.

2 THEORY AND MODEL

The growth rate of the GRTI is given by [Sultan, 1996]

$$\gamma_{RT} = \frac{\Sigma_P^F}{\Sigma_P^F + \Sigma_P^E} \left(V_p - U_L^P - \frac{g_e}{\nu_e^F} \right) K^F - R_T \tag{1}$$

where Σ_p is the Pedersen conductance, V_P is the vertical E × B drift, U_L^P is the F region neutral wind, g_e is gravity, ν_e is the collision frequency, K_F is the inverse density gradient, R_T is the recombination rate in the E region, and the superscripts

E and F refer to the E and F regions. These quantities are flux-tube integrated quantities in the E and F regions as noted by the superscripts. A key point in Eq. (1) is the Pedersen conductance in the denominator; thus, an increase in the E region conductance will reduce the growth rate of the GRTI.

SAMI3 (Sami3 is Also a Model of the Ionosphere) is a seamless, global, three-dimensional, physics-based model of the ionosphere; it is based on SAMI2 [Huba et al., 2000]. Very recently, SAMI3 has been modified to include metallic ions in the E and F regions [Huba et al., 2019]. In particular, the complex transport associated with the electric field and neutral winds in the collisional, lower ionosphere is included. A specialized version of this model (SAMI3/ESF) has been developed to model ESF [Huba et al., 2008] which spans a limited range of longitude and uses a 4th order flux-corrected scheme (the partial donor cell method [Hain, 1978; Huba, 2001]) for cross-field transport which can capture the small-scale (10s km) structure associated with ESF.

The SAMI3/ESF grid used is [nz, nf, nl] = [304,248,256] where nz is number of cells along a magnetic field line, nf is the number of 'magnetic field lines' and nl is the number of longitudes. The latitudinal grid is non-uniform but has a resolution $\lesssim 0.2^{\circ}$ in the low-latitude ionosphere. The grid along the magnetic field is also non-uniform; the spatial resolution in the E region is $\lesssim 2$ km and ~ 4 km in the F-region. The longitudinal grid is uniform with a resolution 0.016° which corresponds to a grid scale ~ 1.8 km. The latitudinal extent of the grid is $\pm 30^{\circ}$, the longitudinal extent is 4° centered about 198° , and the altitude extent is 90 - 2400 km. The simulation was initiated with ionospheric conditions determined from a simulation using the global SAMI3 code. The local time, post-sunset conditions used were centered around 198° .

At t = 0 the metal ions (Mg⁺ and Fe⁺) are uniformly distributed in latitude and longitude with the following distribution

$$n(z) = n_{mi} \exp[(z - z_0)^2 / \Delta z^2]$$
 (2)

where z is the altitude, $z_0 = 105$ km and $\Delta z = 5$ km. This is similar to the observed global average metal ion distribution based on 46 available sounding rocket ion mass spectrometer measurements [Grebowsky and Aikin, 2002]. We consider two metal ion cases with peak densities $n_{mi} = 10^4$ cm⁻³ and $n_{mi} = 10^5$ cm⁻³; a control case is also run with no metal ions for comparison. The geophysical indices used are F10.7 = 114, F10.7A = 129, and Ap = 4 for April 4, 2002. The global SAMI3 model was run for these conditions and used to initialize the SAMI3/ESF model. The global model used NRLMSISE00 [Picone et al., 2002] and HWM14 [Drob et al., 2015] for the neutral composition, temperature, and winds. However, in the SAMI3/ESF runs, the neutral wind is set to $V_n = 0$.

3 RESULTS

We show the Hall and Pedersen conductances as a function of magnetic apex altitude for peak metal ion densities: $n_{mi}=0$, 10^4 , and 10^5 cm⁻³ in Fig. 1. These are the total conductances (i.e., Pedersen and Hall conductivities integrated along the entire magnetic flux tube) and are not separated into E and F region components. We note that the difference in conductances between no metal ions and a metal ion density of $n_{mi}=10^4$ cm⁻³ is relatively small compared to the difference with a metal ion density of $n_{mi}=10^5$ cm⁻³. For the case $n_{mi}=10^4$ cm⁻³ the increase in the Pedersen conductance is $\sim 4\%$ and in the Hall conductance $\sim 50\%$ in the bottomside F region at 300 km. However, for the case $n_{mi}=10^5$ cm⁻³ the increase in the Pedersen conductance is $\sim 20\%$ and in the Hall conductance $\sim 500\%$ at this altitude. Thus, based on Eq. (1) one would anticipate that the growth rate of the GRTI would be somewhat reduced for the case $n_{mi}=10^4$ cm⁻³ but severely reduced for the case $n_{mi}=10^5$ cm⁻³.

In Fig. 2 we show color coded contours of the electron density as a function of longitude and altitude at times LT 19:24 (top), LT 21:22 (middle), and LT 22:03 (bottom). The left panels are for $n_{mi} = 0$, the center panels for $n_{mi} = 10^4 cm^{-3}$, and the right panels for $n_{mi} = 10^5 cm^{-3}$. The metal ion layer is visible at 105 km

in the center and right panels. The plasma is initially perturbed with a sinusoidal perturbation in the F layer (evident in the top panels), and random noise. In the middle panels, at time LT 21:22, the perturbations are still confined to the bottomside of the F peak but the 'topside' altitude of the density depletion at longitude $\sim 198^{\circ}$ decreases as the metal ion density increases. Finally, in the bottom panels at time LT 22:03, the impact of metal ions on ESF is more prominent. For the case of no metal ion layer (left panel), the plasma bubble has bifurcated and penetrated the topside of the F layer; moreover, a bubble has risen to an altitude >600 km. This bubble morphology resembles the bifurcated bubble structure shown in Fig. 5 of Yokoyama et al. (2014). For the case $n_{mi}=10^4~{\rm cm}^{-3}$ (center panel), the bubble has penetrated the topside but has not bifurcated and only risen to an altitude ~ 550 km. The non-bifurcation of the plasma bubble is presumably associated with the enhanced Pedersen and Hall conductances of the metal ion layer. The Hall conductance causes an asymmetry in bubble development while the Pedersen conductance does not. In this case it appears that enhanced Pedersen conductance acts to maintain bubble symmetry as it penetrates the topside and suppress bifurcation. We note that subsequently the bubble does bifurcate at an altitude $\lesssim 600$ km. Finally, for the case $n_{mi} = 10^5$ cm⁻³ (right panel), the density perturbation remains on the bottomside and no large scale plasma bubble develops. Thus, metal ion layers have a stabilizing affect on the GRTI in the equatorial ionosphere, consistent with Eq. (1).

To quantify the results shown in Fig. 2 we present Fig. 3 which plots the maximum upward E × B velocity as a function of time (universal) for $n_{mi} = 0$, 10^4 , and 10^5 cm⁻³. These plots can be used to estimate the growth time τ of the GRTI. There are two phases of growth: a 'slow' phase for $t \lesssim 21$ hrs and a 'fast' phase for $t \gtrsim 21$ hrs (until saturation). The 'fast' phase occurs after the bubble penetrates the F peak, at least for the cases $n_{mi} = 0$ and 10^4 cm⁻³. The growth times τ for the 'fast' (i.e., nonlinear) phase are: $\tau \sim 5$ min for $n_{mi} = 0$ cm⁻³, $\tau \sim 10$ min for 10^4 cm⁻³, and $\tau \sim 52$ min for 10^5 cm⁻³. Additionally we note that the saturated maximum

velocity for the metal ion case $n_{mi} = 10^4 \text{ cm}^{-3}$ is roughly 40% less than the no metal ion case.

The substantial difference in the estimated growth times for the cases $n_{mi} = 10^4$ and 10^5 cm⁻³ suggests that the large increase in the Hall conductance for $n_{mi} = 10^5$ cm⁻³ also plays a role in the suppression of the instability and not just the increase in the E region Pedersen conductance. This is likely due to the reduction (i.e., 'shorting') of the electric field caused by the E region Hall conductance, similar to the disruption of the pre-reversal electric field by sporadic E layers [Abdu et al., 2003]. To test this hypothesis a simulation was conducted for the case $n_{mi} = 10^5$ cm⁻³ with the Hall term set to zero in the potential equation being solved in SAMI3/ESF. In this situation the growth time of the instability was $\tau \sim 35$ min which is $\sim 33\%$ faster than the case when the Hall term is included.

We also investigate the impact of a non-uniform metal ion layer on ESF development. In Fig. 4 we compare the time evolution of the electron density for a uniform metal ion layer (left column) and a non-uniform layer (right column). We consider the metal ion case with $n_{mi} = 10^4$ cm⁻³. The non-uniform case uses the following distribution

$$n(z,\phi) = n_{mi} \exp[(z - z_0)^2 / \Delta z^2] [1 + \cos(2\pi m(\phi - \phi_0) / \Delta \phi)]$$
 (3)

where ϕ denotes longitude, $\phi_0 = 196^\circ$, $\Delta \phi = 4^\circ$, and m = 4. The modulation of the electron density is evident at ~ 105 km in the right column. The top two panels correspond to the times of the bottom two panels in Fig. 2. At time LT 21:22 (top panels) plasma bubbles are forming in the bottomside F layer; however, only a single bubble is forming in the uniform metal ion layer case, while three bubbles are forming in the non-uniform case. At time LT 22:03, a single plasma bubble has penetrated the topside of the F layer in both cases, but multiple bubbles continue to develop in the bottomside for non-uniform metal layer case. Finally, at time LT 22:43 bubbles have risen above 600 km in both cases, but again, the additional bubbles in the non-uniform case continue to develop in the bottomside and are penetrating

the topside of the F layer. Thus, non-uniformities in the E region conductance, associated with inhomogeneous metal ion layers, map to the F region and can affect the morphology of ESF bubble development.

Lastly, we show color contour plots of the Fe⁺ density (\log_{10} cm⁻³) as a function of latitude and altitude at longitude 198° for $n_{mi}=10^4$ cm⁻³ at times LT 21:22, LT 22:03, and LT 23:22 in Fig. 5. Again, the top two panels correspond to the bottom two center panels in Fig. 2. At time LT 21:22, the Fe⁺ are not significantly affected by the instability. However, at times LT 22:03 and LT 23:22 it is found that the Fe⁺ can be lifted into the F region and reach altitudes $\gtrsim 500$ km. This 'lifting' is initially caused by the electric field generated self-consistently by instability within the plasma bubbles. The E × B drift is perpendicular to the magnetic field and has a significant upward vertical component in the low latitude ionosphere. Later in the simulation (i.e., after 23:00 LT), ion motion along the magnetic field plays a role in transporting Fe⁺ to higher and lower altitudes. This is consistent with the observations of Hanson and Sanatani (1971) who report typical Fe⁺ densities $\lesssim 10^2$ cm⁻³ in the F region.

4 SUMMARY

We have investigated the impact of metal ion layers in the E region on the development of equatorial plasma bubbles during ESF using the SAMI3/ESF model. A series of simulations was carried out for peak metal ion densities $n_{mi} = 0$, 10^4 and 10^5 cm⁻³ at an altitude 105 km with a layer half-width of 10 km. We find that metal ion layers reduce the growth rate of the GRTI, inhibiting the development of equatorial plasma bubbles. This is consistent with Eq. (1) as well as observations that sporadic E suppresses ESF [Stephan et al., 2002]. However, in addition to the increase of the E layer Pedersen conductance which appears in the denominator of Eq. (1), the increase in the Hall conductance also plays a significant role in reducing the growth rate of the GRTI. We also find that inhomogeneities in the E region metal ion layer

can map into the F layer and alter the morphology of ESF bubble evolution. Lastly, we find that if equatorial spread F bubbles develop in the presence of a metal ion layer, then the electric fields generated by the instability can lift the metal ions into the F region. Again, this is consistent with observations of Fe⁺ in the F region during equatorial spread F [Hanson and Sanatani, 1971]. These results suggest that metal ion layers may play a role in the day-to-day variability of equatorial spread F.

We have also performed a similar of simulations including the neutral wind using HWM14. The fundamental result remains the same: metal ion layers in the E region can suppress the development of ESF bubbles. However, the actual morphology and structuring of the plasma bubbles are strongly affected by the neutral wind. One other difference is that the zonal wind can 'smear out' any inhomogeneities in the metal ion layer and reduces the impact of these inhomogeneities of F layer structuring.

Acknowledgments: This research was supported by NASA (JDH, JK: NNH17ZDA001N), NSF (JDH: AGS-1931415), and NRL Base Funds (JK, DD). Data available at https://doi.org/10.5281/zenodo.3625979.

References

Abdu, M. A., MacDougall, J. W., Batista, I. S., Sobral, J. H. A., and Jayachandran, P. T., Equatorial evening prereversal electric field enhancement and sporadic E layer disruption: A manifestation of E and F region coupling, J. Geophys. Res., 108, 1254, doi:10.1029/2002JA009285, A6, 2003.

Basu, Su., S. Basu, J.D. Huba, J. Krall, S.E. McDonald, J.J. Makela, E.S. Miller, S. Ray, and K. Groves, Day-to-day variability of the equatorial ionization anomaly and scintillations at dusk observed by GUVI and modeling by SAMI3, J. Geophys. Res. 114, A04302, doi:10.1029/2008JA013899, 2009.

Booker, H.G. and H.G. Wells, Scattering of radio waves by the F-region of the ionosphere, Terr. Mag. Atmos. Elec. 43, 249, 1938.

- de La Beaujardiere, O., C/NOFS: a mission to forecast scintillations, *JASTP*, 66, 1573, 2004.
- Drob, D. P., J. T. Emmert, J. W. Meriwether, J. J. Makela, E. Doornbos, M. Conde, G. Hernandez, J. Noto, K. A. Zawdie, S. E. McDonald, J. D. Huba, and J. H. Klenzing, An update to the Horizontal Wind Model (HWM): The quiet time thermosphere, Earth and Space Science, doi:10.1002/2014EA000089, 2015.
- Grebowsky, J. and A. Aikin, In situ measurements of meteoric ions, in *Meteors in the Earth's Atmosphere*, edited by E. Murad and I.P. Williams, Cambridge University Press, 2002.
- Hanson, W.B. and S. Sanatani, Relationship between Fe⁺ ions and equatorial spread F, J. Geophys. Res., 76, 7761, 1971.
- Haerendel, G., Theory of equatorial spread F, preprint, Max-Planck Inst. für Extraterr. Phys., Munich, Germany, 1974.
- Hain, K. H., The Partial Donor Cell Method, *Journal of Computational Physics*, 1987.
- Haldoupis C., A tutorial review on sporadic E Layers, in: Abdu M., Pancheva D.
 (eds) Aeronomy of the Earth's Atmosphere and Ionosphere, IAGA Special Sopron
 Book Series, vol 2. Springer, Dordrecht, 2011.
- Hanson, W.B. and S. Sanatani, Relationship between Fe⁺ ions and equatorial spread F, J. Geophys. Res., 76, 7761, 1971.
- Huba, J.D. and J.G. Lyon, A new 3D MHD algorithm: the distribution function method, *J. Plasma Phys.* 61, 391, 1999.
- Huba, J.D., G. Joyce, and J.A. Fedder, SAMI2 (Sami2 is Another Model of the Ionosphere): A New Low-Latitude Ionosphere Model J. Geophys. Res., 105, 23,035, 2000.
- Huba, J.D., G. Joyce, and J. Krall, Three-dimensional equatorial spread F modeling, Geophys. Res. Lett. 35, L10102, doi:10.1029/2008GL033509, 2008.
- Huba, J.D. and J. Krall, Impact of Meridional Winds on Equatorial Spread F: Revisited, Geophys. Res. Lett. 40, doi:10.1002/grl.50292, 2013.

- Huba, J.D., J. Krall and D. Drob, Global Ionospheric Metal Ion Transport with SAMI3, *Geophys. Res. Lett.*, 46, doi:10.1029/2019GL083583, 2019.
- Hysell, D.L., An overview and synthesis of plasma irregularities in equatorial spread F, J. Atmos. Sol. Terr. Phys. 62, 1037, 2000.
- Hysell, D. L., M.A. Milla, L. Condori, and J. Vierinen, Datadriven numerical simulations of equatorial spread F in the Peruvian sector 3: Solstice, J. Geophys. Res. Space Physics, 120, 10,809, doi:10.1002/2015JA021877, 2015.
- Krall, J., J.D. Huba, G. Joyce, and S.T. Zalesak, Three-dimensional simulation of equatorial spread F with meridional wind effects, Ann. Geophys. 27, 1821, 2009.
- Maruyama, T. A diagnostic model for equatorial spread F, 1, Model description and application to electric field and neutral wind effects, J. Geophys. Res. 93, 14,611, 1988.
- Nicolet, M., Meteor ionization in the night-time *E* layer, in *Meteors*, ed. T.R. Kaiser, p. 99, Pergamon, New York, 1955.
- Ossakow, S.L., Spread F theories: A review, J. Atmos. Terr. Phys., 43, 437, 1981.
- Picone, J.M., A.E. Hedin, D.P. Drob, and A.C. Aikin, NRLMSISE-00 empirical model of the atmosphere: Statistical comparisons and scientific issues, *J. Geophys. Res.* 107, doi: 10.1029/2002JA009430, 2002.
- Plane, J.M.C., R.M. Cox, and R.J. Rollason, Metallic layers in the mesopause and lower thermosphere region, *Adv. Space Res.*, 24, 1559, 1999.
- Richards, P.G., J.A. Fennelly, and D.G. Torr, EUVAC: A Solar EUV Flux Model for Aeronomic Calculations, J. Geophys. Res. 99, 8981, 1994.
- Richmond, A., Ionospheric electrodynamics using magnetic apex coordinates, *J. Geomag. Geoelec.* 47, 191, 1995.
- Stephan, A.W., M. Colerico, M. Mendillo, B.W. Reinisch, and D. Anderson, Suppression of equatorial spread F by sporadic E, J. Geophys. Res., 107, 1021, 2002.
- Sultan, P.J., Linear theory and modeling of the Rayleigh-Taylor instability leading to the occurrence of equatorial spread F, J. Geophys. Res. 101, 26,875, 1996.
- Yokoyama, T., H. Shinagawa, and H. Jin, Nonlinear growth, bifurcation and pinching of equatorial plasma bubble simulated by three-dimensional high-resolution bubble

 $\label{eq:model} \mbox{ model, J. $Geophys. $Res.$: $Space Physics, 119, $10,474$, $\mbox{doi:}10.1002/2014JA020708$, 2014.}$

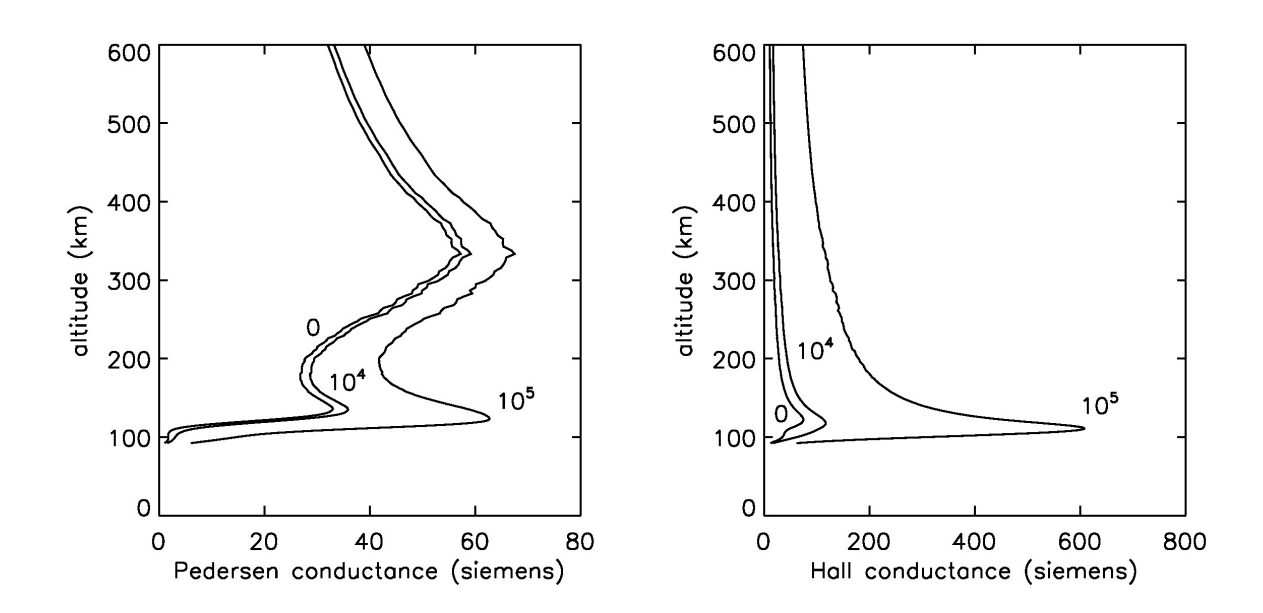


Figure 1: Pedersen (left) and Hall (right) conductances as a function of magnetic apex altitude for peak metal ion densities: $n_{mi} = 0$, 10^4 , and 10^5 cm⁻³.

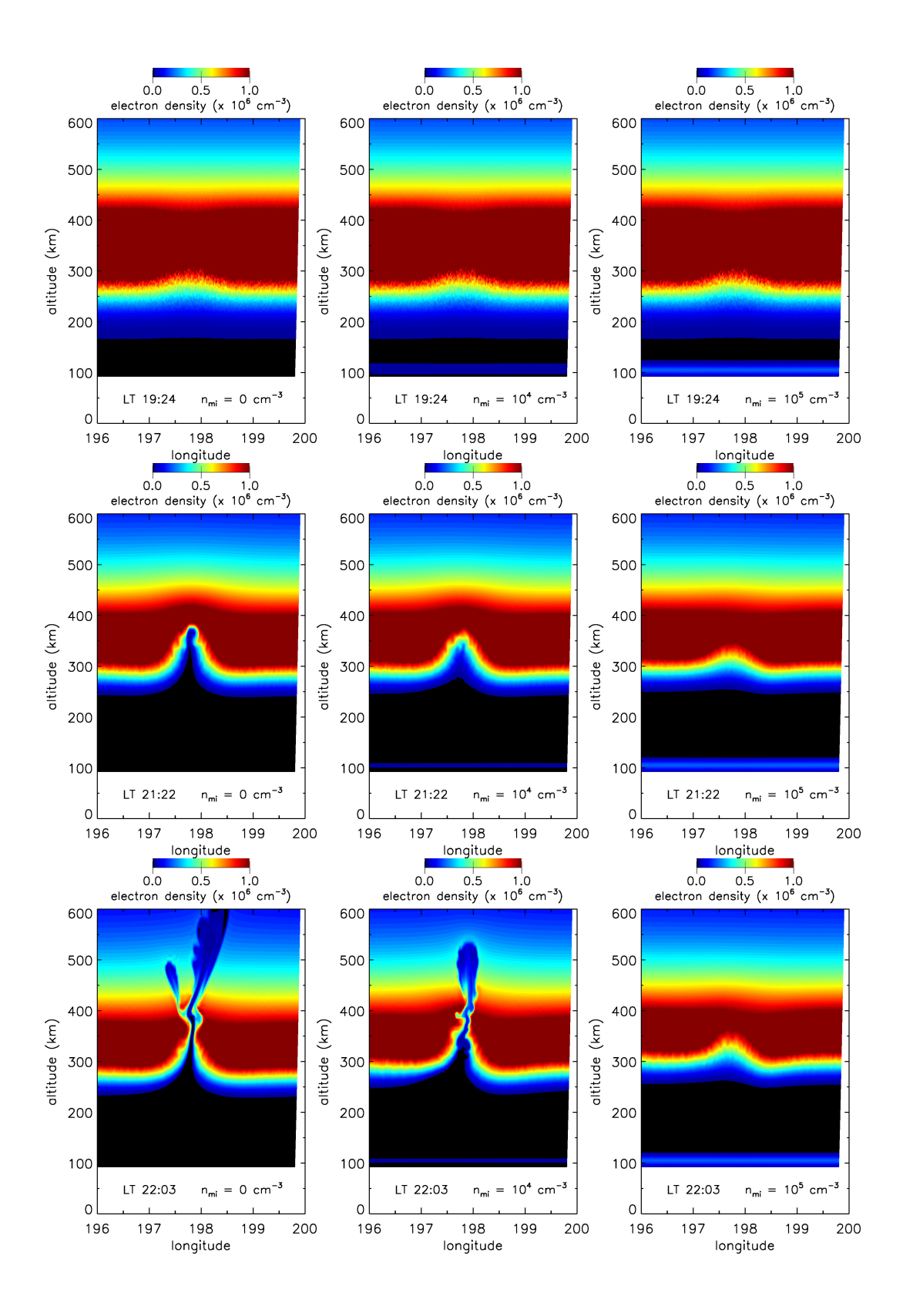


Figure 2: Color coded contours of the electron density as a function of longitude and altitude at times LT 19:24, LT 21:22, and LT 22:03. The left panels are for $n_{mi} = 0$ cm⁻³, the center panels for $n_{mi} = 10^4$ cm⁻³, and the right panels for $n_{mi} = 10^5$ cm⁻³.

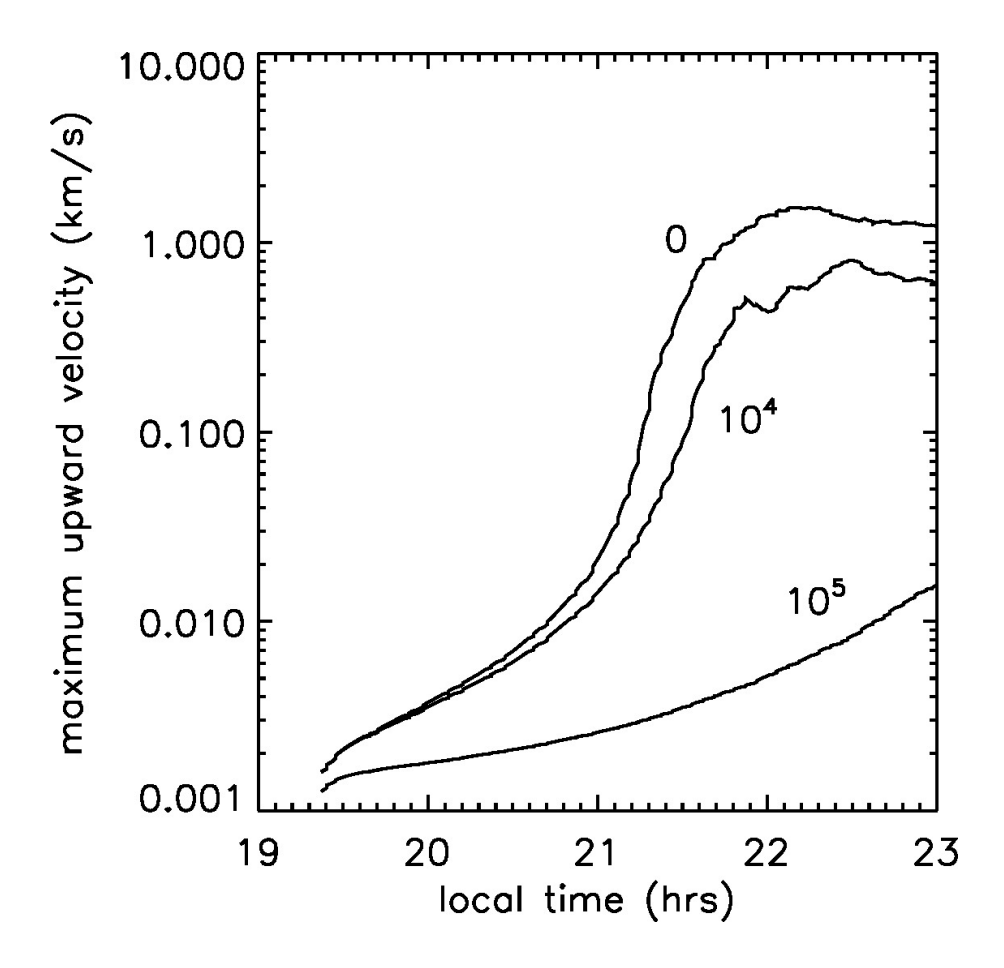


Figure 3: The maximum upward E \times B velocity as a function of universal time for $n_{mi}=0,\,10^4,\,{\rm and}\,\,10^5~{\rm cm}^{-3}.$

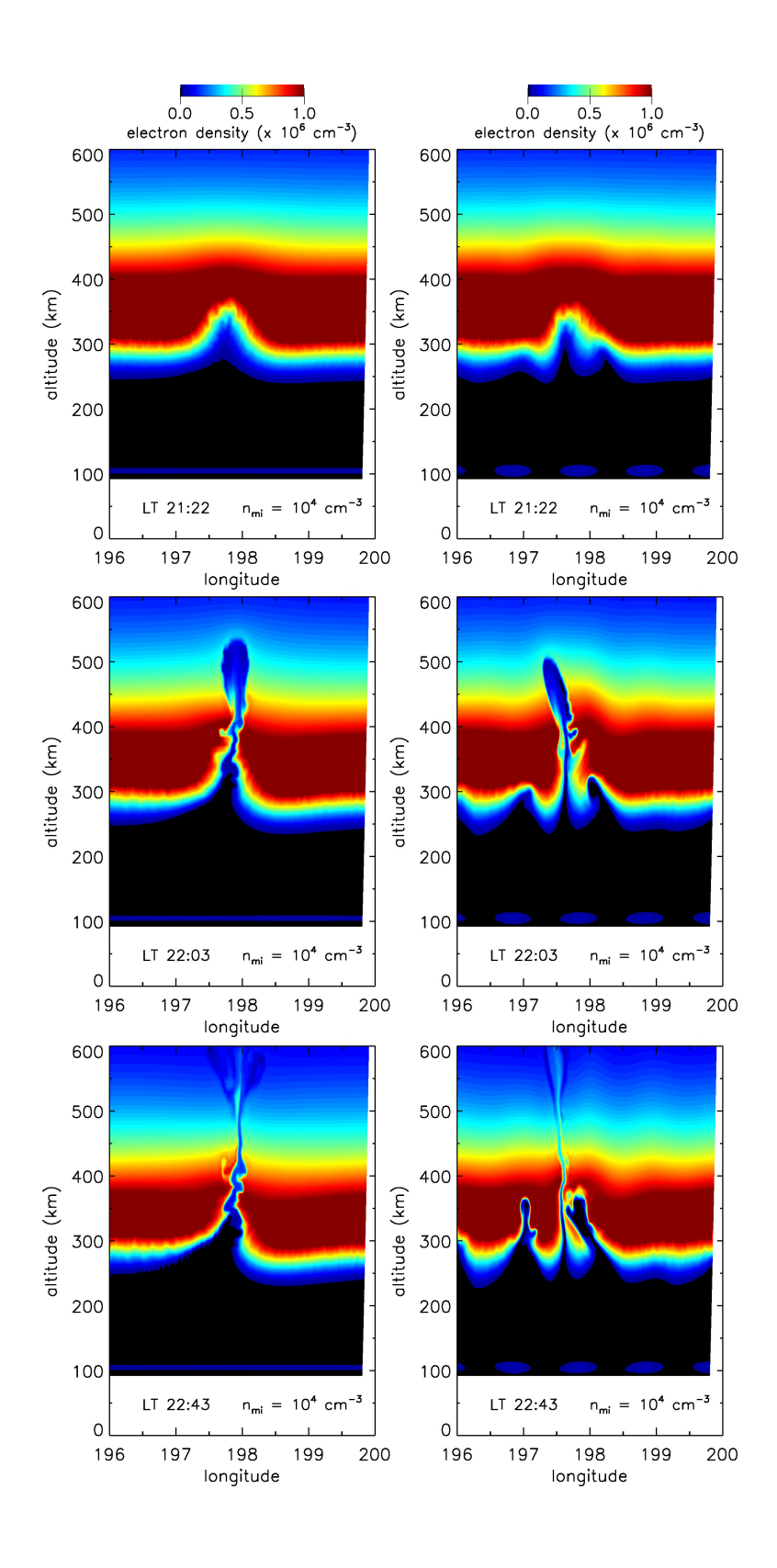


Figure 4: Color coded contours of the electron density as a function of longitude and altitude at times LT 21:22, LT 22:03, and LT 22:43 for $n_{mi} = 10^4$ cm⁻³: uniform metal ion layer (left column) and non-uniform metal ion layer (right column).

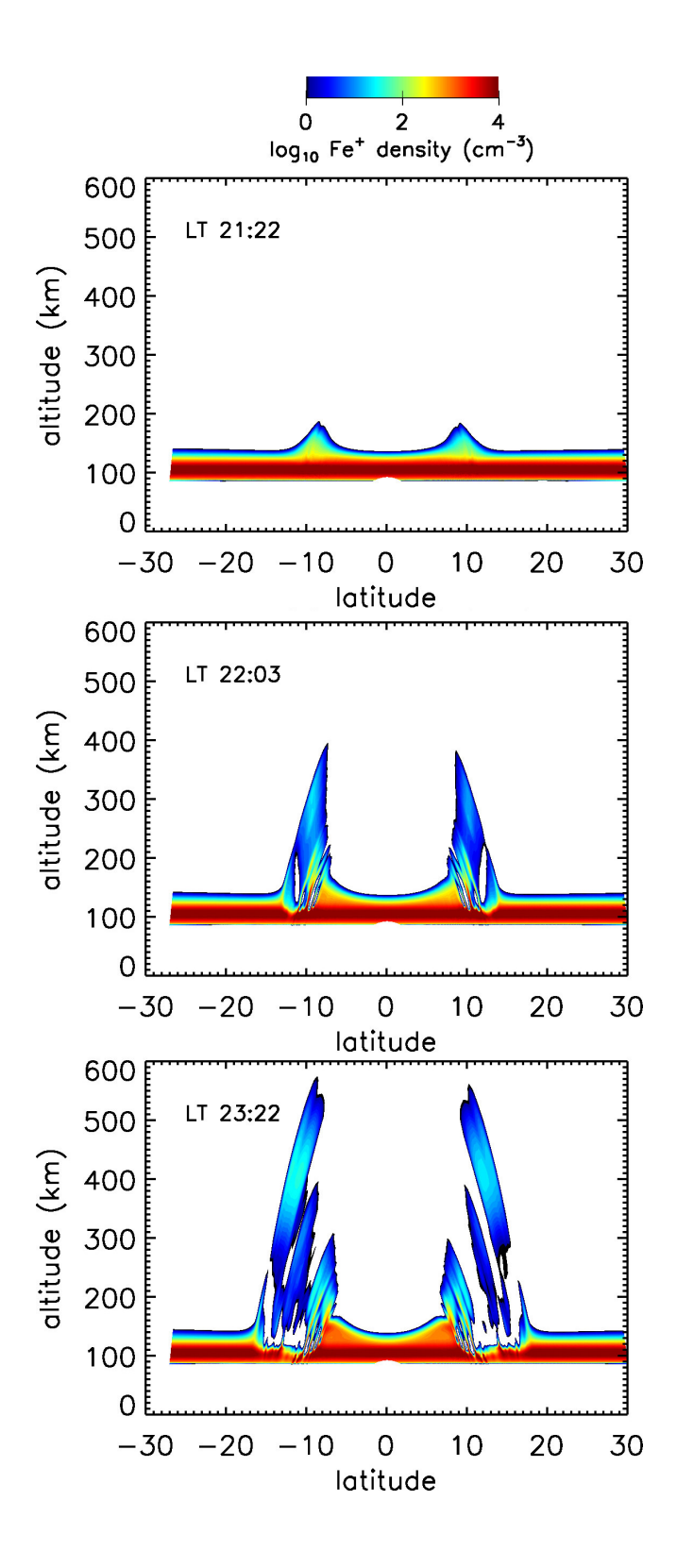


Figure 5: Color contour plots of the Fe⁺ density (\log_{10}) as a function of latitude and altitude at longitude 198° for $n_{mi}=10^4~{\rm cm}^{-3}$ at times LT 21:22, LT 22:03, and LT 23:22.